




Article

Effect of MAF-6 Crystal Size on Its Physicochemical and Catalytic Properties in the Cycloaddition of CO₂ to Propylene Oxide

Maria N. Timofeeva ^{1,2,*} , Ivan A. Lukoyanov ^{1,2}, Valentina N. Panchenko ^{1,2}, Biswa Nath Bhadra ³, Evgenii Yu Gerasimov ¹  and Sung Hwa Jhung ^{3,*} 

- ¹ Boreskov Institute of Catalysis SB RAS, Prospect Akad. Lavrentieva 5, 630090 Novosibirsk, Russia; ivan_lukoyanov95@mail.ru (I.A.L.); panchenko@catalysis.ru (V.N.P.); gerasimov@catalysis.ru (E.Y.G.)
² Novosibirsk State Technical University, Prospekt K. Marksa 20, 630092 Novosibirsk, Russia
³ Department of Chemistry and Green-Nano Materials Research Center, Kyungpook National University, Dae Hak-Ro 80, Buk-Ku, Daegu 41566, Korea; bbhadra1981@gmail.com
* Correspondence: timofeeva@catalysis.ru (M.N.T.); sung@knu.ac.kr (S.H.J.);
Tel.: +7-383-330-7284 (M.N.T.); +82-53-950-5341 (S.H.J.)

Abstract: Zeolitic imidazolate frameworks MAF-5 and MAF-6 based on Zn²⁺ and 2-ethylimidazole were demonstrated to be efficient heterogeneous catalysts in solvent-free coupling of CO₂ and propylene oxide (PO) to produce propylene carbonate (PC) at 0.8 MPa of CO₂ and 80 °C. Activity of MAF-5 was lower in comparison with MAF-6 due to the difference in their structural and textural characteristics. MAF-6 samples with particle size of 190 ± 20, 360 ± 30, and 810 ± 30 nm were prepared at room temperature from [Zn(NH₃)₄](OH)₂ and 2-ethylimidazole. Control of particle size was achieved by variation of type of alcohol in alcohol/cyclohexane media for the preparation of MAF-6. According to this comprehensive study, the yield of PC was found to decrease with increasing crystal size of the MAF-6 material, which was related to the change in textural properties and the number and localization of active sites. The combination of MAF-6 with particle size of with particle size of 190 ± 20 nm and tetrabutylammonium bromide ([n-Bu₄N]Br) as co-catalyst led to an approximately 4-fold enhancement in the yield of PC (80.5%). Compared with reported ZIFs catalysts, the efficiencies of MAF-5/[n-Bu₄N]Br and MAF-6/[n-Bu₄N]Br binary systems were comparable and higher under similar reaction conditions.

Keywords: zinc zeolitic imidazolate frameworks; MAF-5; MAF-6; effect of particle size; cycloaddition; CO₂; propylene carbonate; propylene oxide



Citation: Timofeeva, M.N.; Lukoyanov, I.A.; Panchenko, V.N.; Bhadra, B.N.; Gerasimov, E.Y.; Jhung, S.H. Effect of MAF-6 Crystal Size on Its Physicochemical and Catalytic Properties in the Cycloaddition of CO₂ to Propylene Oxide. *Catalysts* **2021**, *11*, 1061. <https://doi.org/10.3390/catal11091061>

Academic Editor: Gang Li

Received: 10 August 2021

Accepted: 30 August 2021

Published: 31 August 2021

Publisher's Note: MDPI stays neutral with regard to jurisdictional claims in published maps and institutional affiliations.



Copyright: © 2021 by the authors. Licensee MDPI, Basel, Switzerland. This article is an open access article distributed under the terms and conditions of the Creative Commons Attribution (CC BY) license (<https://creativecommons.org/licenses/by/4.0/>).

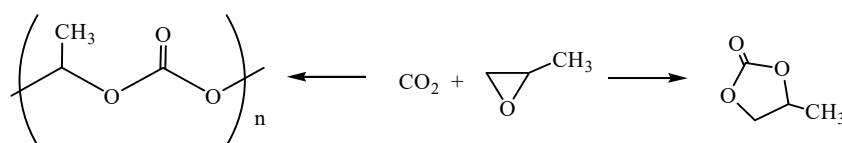
1. Introduction

Nowadays, it is nearly impossible to imagine modern life without the products of chemistry. The chemicals industry and other related industries supply us with a huge variety of essential products, from plastics to pharmaceuticals. However, these industries are based on the utilization of fossil fuels as a source of energy and feedstocks, and often release pollutants into the environment that provokes both economic and environmental challenges. Moreover, due to the technological progress and rapid expansion of the population in the World since the second half of the 20th century immediate availability would no longer be able to fulfill the increasing global demand for these raw materials. To use renewable carbon resources, i.e., biomass and CO₂, in the chemical and energy industries, it is a key to finding lasting solutions to both economic and environmental challenges.

Carbon dioxide is a waste product from all combustion processes and many chemical industries. CO₂ represents a potential and alternative carbon feedstock for the preparation of a variety of useful chemicals [1–4]. Several routes having a significant potential for both the chemical utilization of large amounts of CO₂ and becoming economically profitable were pointed in the position paper «Utilization and storage of CO₂» [5]. The application

of CO₂ for the synthesis of polymer, fuel, and chemicals is one of these routes. Currently, there are few industrial processes that utilize CO₂ as a raw material into value-added chemicals [6,7]: there are the methods for the commercial synthesis of urea from CO₂ and ammonia (190 million tons produced worldwide in 2020 [8]) and the Kolbe–Schmitt synthesis of salicylic acid from CO₂ and phenol (102,812 kilotons produced worldwide in 2017 [9]). Methods for the commercial synthesis of cyclic carbonates and polycarbonates from CO₂ and epoxides in the presence of basic catalysts were developed in 1950 [1,4,10]. Approximately 6.0 million tons of polycarbonates per year is obtained by the Asahi–Kasei process [10]. Recently, Covestro developed a plant for the copolymerization of CO₂ with propylene oxide to generate polymeric polyols (polyether carbonates), branded as Cardyon [11]. These polyols are used to make polyurethanes, which are found in foam mattresses. Cyclic carbonates are produced on a smaller scale. The ethylene carbonate market was valued at \$288.0 million in 2019 and is projected to \$418.5 million by 2027 [12]. The propylene carbonate market was valued at US\$ 454.0 million in 2018, and it is projected to increase by 6.2% from 2019 to 2028 [13]. Note that the five-membered cyclic carbonates are widely used as lubricants, surface coatings, plasticizers, lithium battery electrolytes, solvents, selective reagents, fuel additives, monomers for polymers, and intermediates in the production of pharmaceuticals and other fine chemicals [4,10,14,15].

The reaction of propylene oxide (PO) with CO₂ can in principle yield two possible products: a five-membered cyclic carbonate (propylene carbonate, PC) and/or a polymeric carbonate (polypropylene carbonate, PPC) (Scheme 1). The catalytic systems that are used to promote this reaction generally consist of a Lewis base acting as a nucleophile and a Lewis acid species in the form of one or more metal centers.



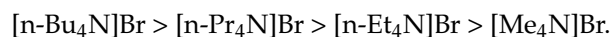
Scheme 1. Reaction between propylene oxide and carbon dioxide to propylene carbonate (PC; right) and polypropylene carbonate (PPC; left).

There have been many different types of homogeneous and heterogeneous catalysts suggested for the synthesis of PC via the coupling reaction of carbon dioxide with PO. Yano et al. [16] demonstrated that a commercial MgO could give PC with 41% yield at 135 °C and 2 MPa of CO₂ for 12 h in a solvent of dimethylformamide. According to the work in [17], the catalytic efficiency of MgO was higher in comparison with ZnO, ZrO₂, La₂O₃, CeO₂, CaO, and Al₂O₃. In the presence of MgO a yield of PC was 32% with a 92% selectivity at 150 °C and 8 MPa of CO₂ for 15 h. At the same time, a higher PC yield of 54% and lower selectivity (75%) were observed in the presence of La₂O₃. These differences were explained by a large amount of moderately basic sites in MgO.

The coupling reaction of carbon dioxide with PO to produce PC was also efficiently catalyzed by ionic liquids (ILs) based on large organic cations like imidazolium, ammonium, pyridinium ones, and inorganic anions [18–20] and systems based on immobilized ILs [21]. Type of cation and anion affect the reaction rate and selectivity towards PC [22]. In the case of 1-*n*-butyl-3-methylimidazolium (BMIM) derivatives, high conversion and selectivity were found to be observed in anions with Br[−] and I[−], while relatively low selectivity was observed in the cases of BMIM with Cl[−], AcO[−], HCO₃[−], malonate, and proline. The high activity of systems based on ILs was explained by the interaction between the imidazolium ring proton at the C2-position and the epoxide oxygen atom that make easy epoxide ring-opening in the course of nucleophilic attack of Br[−] on the C atom of PO.

Metal–organic frameworks (MOFs)—materials fabricated by metal ions/clusters and organic ligands—were also found to catalyze the reaction between CO₂ and PO [23,24]. The catalytic activity of MOFs systems resulted in the high CO₂ adsorption capacity on the active sites, which are due to the defect sites within or on the surface of the crystalline mate-

rials. According to the work in [25], the addition of the quaternary ammonium salts (QAS) to MOF-5 leads to an increase in yield of PC in the presence of MOF-5/[QAS]Br binary system, and the yield of PC increases with the alkyl chain length in the following order:



In optimal experimental conditions (6 MPa, 50 °C, 4 h), the yield of PC was 95.5% in the presence of MOF-5/[n-Bu₄N]Br. Notable that this binary system could be used for three cycles without loss in activity.

Zeolitic imidazolate frameworks (ZIFs), as a sub-class of MOFs, were also reported as efficient catalysts in the cycloaddition of CO₂ to PO [23,24]. ZIFs are porous crystals with zeolite-type tetrahedral topologies, which are constructed from tetrahedral metal ions (Zn²⁺, Co²⁺, Fe²⁺, etc.) bridged by imidazolate ligands. ZIFs combine the benefits of zeolites and MOF materials: high chemical and thermal stabilities, uniform pore distribution, and high specific surface area and microporosity. ZIFs draw attention as catalysts due to the availability of Zn²⁺ (as Lewis acidic sites, LAS) and imidazolate linkers (as basic sites, BS) in the structure. Some especially noticeable features of ZIFs are high hydrophobicity and excellent capability for CO₂ adsorption and capture. Nowadays, a series of ZIFs and ZIFs/[n-Bu₄N]Br binary systems were reported (Tables 1 and 2) [26–33]. The yield of cyclic carbonate was 49–81% with 95–99% selectivity in the presence of ZIF-23, ZIF-90, ZIF-90, F-ZIF-90, and ZIF-95 at 0.8–1.2 MPa of CO₂ and 100–140 °C (Table 1). The yield of PO was significantly enhanced in the presence of mixed CoZn-ZIF composite due to the synergistic effect of Lewis acid–base by comparing the catalytic performance of ZIF-8(Zn) and ZIF-67(Co) (Table 1). Park et al. [32] suggested that this phenomenon was resulted in exploiting the advantageous properties of Zn (high activity) and Co (low leaching and high selectivity). The addition of co-catalyst favors the increasing catalytic efficiency of ZIFs that allows reducing reaction rate and pressure of CO₂. Thus, high activity of ZIF-23/[n-Bu₄N]Br [27] and ZIF-95/[n-Bu₄N]Br [31] binary systems was observed at 80–100 °C and 1.2 MPa (Table 2).

Table 1. Cycloaddition of CO₂ to propylene oxide in the presence of ZIFs without co-catalyst.

Catalyst	Experimental Conditions					Catalytic Test		Ref.
	(mmol) ^a	PO (mmol)	P _{CO₂} (MPa)	T (°C)	Time (h)	PO Conversion (%)	PC Yield (%)	
MAF-6(L)	0.85	24.0	0.8	80	5	8.0	7.9	This work
MAF-6(M)	0.85	24.0	0.8	80, 100	5	12.2, 34.1	11.0, 33.8	This work
MAF-6(S)	0.85	24.0	0.8	80	5	22.3	22.0	This work
MAF-5	0.85	24.0	0.8	80	5	8.3	8.2	This work
ZIF-8	0.52	25	1.0	110	3	<5	<5	[26]
ZIF-23	0.8	42.9	3.0	140	24	71.2	70.3	[27]
ZIF-90	0.52	42.9	1.2	90, 120	8	13, 88	11, 81	[28]
ZIF-90	0.49	18.1	1.0	120	3	51.0	49.0	[29]
F-ZIF-90	0.177	18.1	1.2	120	6	89	87.8	[30]
ZIF-95	0.4	18.6	1.2	80	24	91.0	90	[31]
CoZn-ZIF	0.7	25	0.7	100	4	81	99	[32]

^a Amount of catalyst based on PO.

Table 2. Cycloaddition of CO₂ to propylene oxide in the presence of ZIFs/[n-Bu₄N]Br binary systems.

Catalytic System	Experimental Conditions					Catalytic Test		Ref.	
	(mmol) ^a	[n-Bu ₄ N]Br (mmol) ^a	PO (mmol)	P _{CO2} (MPa)	T (°C)	Time (h)	PO Conversion (%)		PC Yield (%)
MAF-6(L)	0.85	0.85	24	0.8	80	5	65.0	64.3	This work
MAF-6(M)	0.85	0.85	24	0.8	80	5	67.6	67.2	This work
MAF-6(S)	0.85	0.85	24	0.8	80	5	80.5	79.6	This work
MAF-5	0.85	0.85	24	0.8	80, 100	5	67.3, 80.7	66.6, 79.9	This work
ZIF-23	0.8	0.8	42.9	1.2	80, 100, 120	6	55.6, 58.8, 61.9	55, 58.2, 61.3	[27]
ZIF-95	0.4	0.4	18.6	1.2	80, 100	2	83.2, 97.2	84.0, 96.2	[31]
MOF-5	2.5	2.5	20.0	6	50	4	-	97.6	[25]
UMCM-1-NH ₂	0.64	0.64	42.8	1.2	RT	24	90	90	[33]

^a Amount of catalyst and [n-Bu₄N]Br based on PO.

Recently, Chen et al. [34] demonstrated that the reaction rate of cycloaddition between CO₂ and styrene oxide could be tuned easily by the morphology control synthesis of ZIF-8. Morphology of ZIF-8 was found to affect the porosity and the number of acidic and basic sites and, therefore, catalytic performance. The activity of ZIF-8 decreased in the following order:

solid spheres > hollow spheres > hierarchical particles
> stackable particle > nano-dodecahedrons.

The high activity of ZIF-8 solid spheres was due to its highest specific surface areas, most abundant acid–basic sites, and large mesoporous volume. The effect of the morphology of ZIF-8 particles was also demonstrated for the condensation reaction of 4-bromobenzaldehyde (BA-Br) with malononitrile [35]. The conversion of BA-Br for 30 min of the reaction decreased in the following order:

truncated rhombic dodecahedron (141 ± 48 nm) > rhombic dodecahedron (500 nm) > cubes and a rhombic dodecahedron (~1050 nm).

This order was explained by the decrease in the number of available active sites due to a decrease in the area of the outer surface of ZIF-8 crystals. A similar effect of morphology and particle size of ZIF-8 was also demonstrated by Zhang et al. [36] for [3+3] cycloaddition reactions between dions and aldehydes.

We have recently studied the effect of ZIF-8 particle size (50–800 nm) in a hexagonal shape on their catalytic efficiency in the synthesis of propylene glycol methyl ether (PGME) from PO and methanol [37,38]. A pronounced size effect on the reaction rate and selectivity toward PGME was found to decrease along with the growth of the ZIF-8 crystal size. According to the physicochemical investigations, this phenomenon was explained by the change in textural characteristics and the surface-to-volume ratio of the number of the basic sites. Note that reaction rate and selectivity towards PGME depended also on the type of ZIFs (Table S1, Supporting Information) and decreased in the following order:

MAF-5 (ZIF-71) > MAF-6 (ZIF-14) > ZIF-8.

This correlation was caused by the increasing channel size and decreasing surface basicity of ZIFs [38,39].

Herein, we present an investigation of the catalytic properties of MAF-5 and MAF-6 in the coupling reaction of carbon dioxide with PO to produce PC. The main attention was focused on the examination of the effect of the MAF-6 catalyst crystallite size on its catalytic performance, because the reduction of the particle size from the micrometer to the nanometer scale could involve changes in its physicochemical and catalytic properties. A combination of catalytic and physicochemical methods was used for solving such a challenge. Thus, the nature of the active sites of the MAF-6 samples was analyzed by DRIFT spectroscopy using CDCl₃ as a probe molecule and DR-UV-Vis spectroscopy. Morphology

and particle size were analyzed by SEM and XRD methods. We assume that investigation of size effect could open the way for the tuning and control catalytic properties of MAF-6, in particular, and ZIFs, in general, in this reaction.

2. Results and Discussion

2.1. Synthesis and Characterization of MAF-6 and MAF-5

MAF-5 was synthesized at room temperature with 2-EIM/ Zn^{2+} molar ratio of 2.0 in methanol solution. A combination of physicochemical methods points to the formation of the MAF-5 structure with high crystallinity [39]. SEM images, XRD pattern and textural characteristics are shown in Figures S1–S3 (Supporting Information) and Table 3.

2.1.1. Structural and Textural Properties of MAF-6

The zeolitic imidazolate framework MAF-6s with different particle sizes were synthesized from $[Zn(NH_3)_4](OH)_2$ and 2-EIM. The particle size estimated by SEM was tuned by the changing of solvent type (Table 3). Microscopy images of MAF-6 samples are shown in Figure 1. One can see that all samples have uniform particle size distributions. The morphology of crystals is a rhombic dodecahedron structure exposing 12{110} faces. The experimental data (Table 3) show the particle size of MAF-6 decreases in the following order, because of solvent effect:



Earlier, the effect of solvent on the crystallization rate and size of crystal was demonstrated for ZIF-8 [40]. Similar to our results, the crystal size of ZIF-8 was demonstrated to decrease in the following order:



Table 3. Synthesis, abbreviation, textural properties, and crystal sizes of ZIFs.

Experimental Conditions				Textural Properties				
	Solvent		α^a	Crystal Size ^b (nm)	S_{BET} (m ² /g)	V_{Σ} (cm ³ /g)	V_{μ} (cm ³ /g)	V_{μ}/V_{Σ}
	(vol./vol.)							
MAF-6(S)	PrOH/cyclohexane	28.5:1.5	0.84	190 ± 20	1258	0.59	0.43	0.73
MAF-6(M)	EtOH/cyclohexane	28:2	0.86	360 ± 30	1395	0.71	0.58	0.82
MAF-6(L)	MeOH/cyclohexane	27:3	0.98	810 ± 30	1579	0.68	0.63	0.93
MAF-5	MeOH	-	-	190–260	464	0.32	0.17	0.53

^a α —Value of a hydrogen bond donation of solvents; Value of HBD for cyclohexane is 0 [41]. ^b Measured from series of SEM images.

The impact of solvent was explained by its role as a structure-directing agent via its included in the framework by non-covalent interactions that can be confirmed by the correlation between crystal size of ZIF-8 and value of the hydrogen bond donation of solvents (α) [41]. Park et al. [42] also suggested the interaction between solvent and framework of ZIF-8 that followed from the presence of solvent molecules near the hydrogen atoms of 2-methylimidazolate groups.

The XRD patterns of the MAF-6 samples with different particle sizes are shown in Figure 2. The observed characteristic diffraction peaks of RHO structure with crystalline peaks at diffraction angles (2θ) 5.90°, 7.28°, 8.44°, and 9.44° displayed similar XRD patterns of MAF-6 reported in the literature [43–45]. The average crystal size of MAF-6 samples was calculated from X-ray spectra using the Debye–Scherrer equation (Equation (1)) [46,47]:

$$D_{XRD} = \frac{0.9 \cdot \lambda}{\beta \cdot \cos \theta} \quad (1)$$

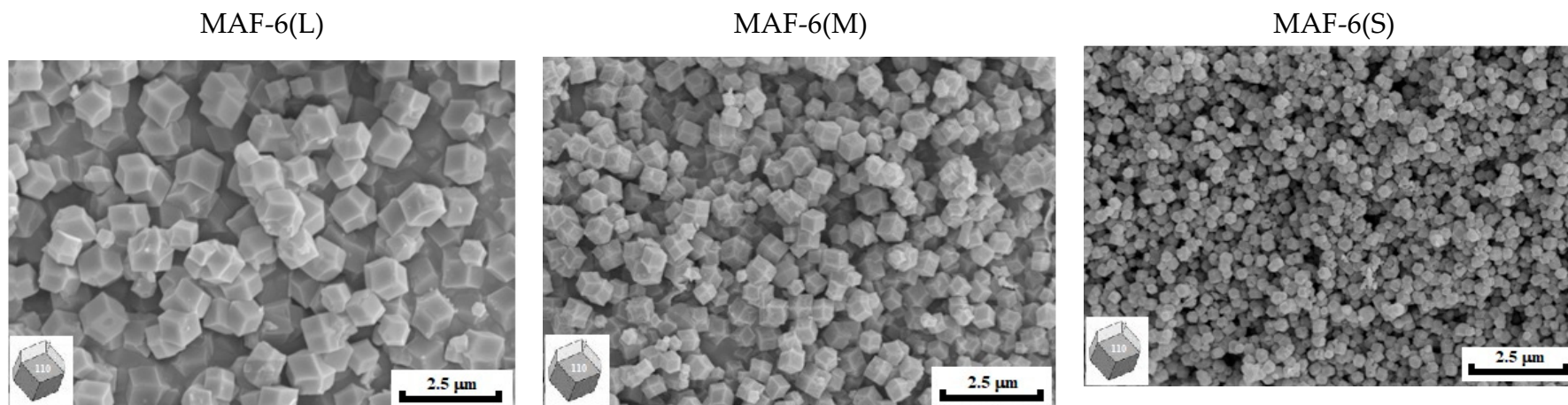


Figure 1. SEM images of MAF-6 samples with different particle sizes.

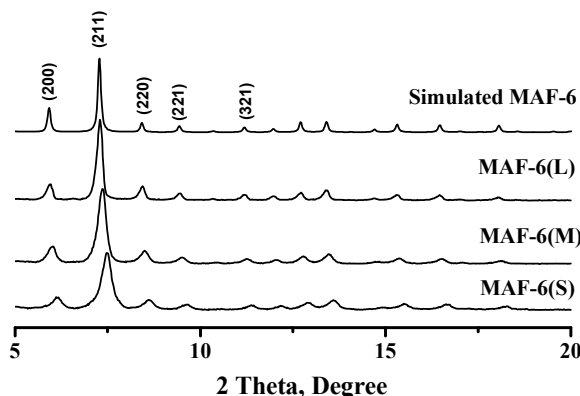


Figure 2. XRD patterns of MAF-6 with different particle sizes.

Where D_{XRD} is particle size (nm), β is the full-width at half maximum of the peak (radian), Θ is the Bragg angle of diffraction peak (grad), and λ is X-ray wavelength of $\text{CuK}\alpha$ (0.1542 nm). The D_{XRD} value for MAF-6 was found to change in the following order (Table S2, Supporting Information):

$$\text{MAF-6(L)} (36 \pm 2 \text{ nm}) > \text{MAF-6(M)} (29 \pm 2 \text{ nm}) > \text{MAF-6(S)} (24 \pm 1 \text{ nm}).$$

If we assume that MAF-6 particles consist of domains and the size of each domain is equal to that of the region of X-ray coherent scattering (D_{XRD}), the D_{SEM}/D_{XRD} ratio can be considered as a parameter indicating the relationship between regular and imperfect structural regions in the bulk of the MAF-6 particle (Table S2, Supporting Information). The data suggest that the size of imperfect structural regions rises with decreasing particle size (D_{SEM}/D_{XRD}):

$$\text{MAF-6(L)} (23) < \text{MAF-6(M)} (12) < \text{MAF-6(S)} (10)$$

Textural properties of MAF-6 samples are shown in Table 3. It was found that the specific surface area and microporosity (V_{μ}/V_{Σ}) of MAF-6 increased with increasing crystal size. This phenomenon can be explained by the impact of the nature of alcohols used in MAF-6 synthesis on the formation of pore structure. First, both basicity of solvent and size of molecule of solvent are important for the hydrogen bonding interaction between the alcohol and 2-MIM, i.e., the linker deprotonation, because this interaction affects the rate of nucleation and crystal growth. Moreover, molecules of alcohol can be incorporated in the as-synthesized MAF-6 structure and act as a space-filling molecule as kinetic diameters of alcohols (MeOH 3.8 Å, EtOH 4.30 Å and n-PrOH 4.7 Å [48]) are smaller in comparison with the pore size of MAF-6 (theoretical pore size: 7.6 Å [49]). Note that the effect of particle size on the textural properties was demonstrated for ZIF-8 [37,50,51]. It was also found that the external surface decreases, while microporosity increases with increasing crystal size.

2.1.2. Nature of Active Sites of MAF-6

The nature and structure of active sites were investigated by different spectral methods, such as DRIFT spectroscopy, DR-UV-Vis spectroscopy, and DRIFT spectroscopy using CDCl_3 as a probe molecule.

DRIFT spectroscopy. The DRIFT spectra of MAF-6 samples with different particle sizes are shown in Figures 3 and S5 (Supporting Information). In spectra of samples, the bands observed in the regions of 3650–3300 cm^{-1} and 1550–1650 cm^{-1} may be attributed to the $\nu_{(\text{OH})}$ stretching mode of water and alcohol molecules [52–54]. The 2-ethylimidazole has bands in the region of 2800–3150 cm^{-1} and at 1152 cm^{-1} which are assigned to the $\nu_{(\text{CH}_3)}$ and $\nu_{(\text{CH}_2)}$ asymmetric and symmetric stretching frequencies and $\rho_{(\text{CH}_2)}$ in-plane rocking vibration frequency, respectively. Moreover, the $\delta_{(\text{CH}_3)}$ in-plane and $\omega_{(\text{CH}_3)}$ out of plane bending modes are observed at 1172 and 1143 cm^{-1} in the DRIFT spectrum, respectively.

The observed bands at 1470 and 1454 cm^{-1} are assigned to $\nu_{(\text{C}-\text{N})}$ stretching vibration in 2-ethylimidazole ligand. The band in the region of 410 to 440 cm^{-1} is particularly worth discussing. This band is assigned to the Zn-N stretching mode due to the interaction between a Zn atom and an N atom of 2-ethylimidazole. In a spectrum of MAF-6(L), a symmetric band at 423 cm^{-1} is observed. At the same time, this band splits to 418 and 434 cm^{-1} in spectra of MAF-6(M) and MAF-6(S), respectively. We can suggest that band at 434 cm^{-1} is attributed to the Zn-O stretching mode due to the interaction between the Zn^{2+} ions of MAF-6 and the oxygen atom of alcohol [37,39]. The change in the character of bands in the region of 770–790 cm^{-1} (OH out-of-plane bend) (Figure 3) and 1300–1330 cm^{-1} (OH in-plane bend) (Figure S5, Supporting Information) point also to this interaction.

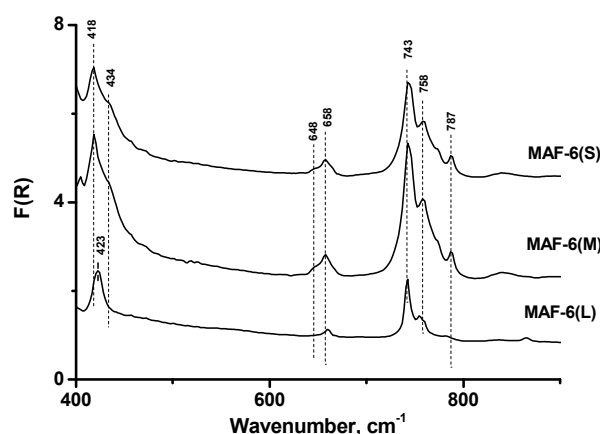


Figure 3. DRIFT spectra of MAF-6 with different particle sizes.

DR-UV-Vis spectroscopy. DR-UV-Vis spectra of MAF-6 samples are shown in Figures 4A and S6 (Supporting Information). Two types of bands are observed in spectra of samples:

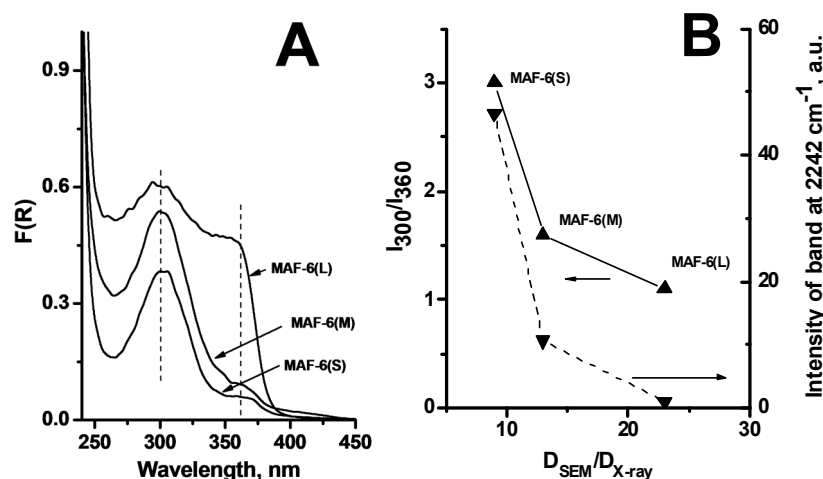


Figure 4. (A) DR-UV-Vis spectra of MAF-6 samples with different particle size. (B) Correlation between data of DR-UV-Vis (I_{300}/I_{360}), DRIFT- CDCl_3 spectroscopy (I_{2242}) and $D_{\text{SEM}}/D_{\text{X-ray}}$.

- (1) Internal ligand charge transfer $\pi \rightarrow \pi^*$ in the region of 205–235 nm [55,56];
- (2) Charge-transfer ligand-to-metal (LMCT) $n \rightarrow \text{Zn}^{2+}$ (the highest energy $n1_{\text{EMIM}} \rightarrow \text{Zn}^{2+}$ (λ_{max} 300 nm) and lower energy $n2_{\text{EMIM}} \rightarrow \text{Zn}^{2+}$ (λ_{max} 360 nm)) in the region of 250–400 nm.

Ideally, Zn^{2+} ion bounds to the four ligands via nitrogen atoms in the structure of ZIFs (Zn_{IV} atoms). However, DFT calculations [57,58] pointed that ZIF-8 can have low-coordinated Zn atoms (Zn atoms without one or two linkers, Zn_{III} and Zn_{II} atoms), and

free N-moieties belonging to linkers can exist on the external surface of solid. For the identification of λ_{300} and λ_{360} bands, the following points should be taken into account:

(1) The energy of ligand-to-metal charge transfer depends on the coordination of zinc atoms in the samples.

(2) The increasing integral intensity of the band at 300 nm in DR-UV-Vis spectra of MAF-6 samples after heating under vacuum at 150 °C for 6 h and the next increasing after wet air addition (Figure S6, Supporting Information).

Therefore, λ_{300} and λ_{360} bands can be ascribed to the metal-to-ligand charge transfer from low-coordinated Zn atoms (Zn_{III} and Zn_{II}) to ligand and high-coordinated Zn atoms (Zn_{IV}) to ligand, respectively. This suggestion agrees with the correlation between D_{SEM}/D_{XRD} ratio and the ratio of intensities of λ_{300} and λ_{360} (I_{300}/I_{360}) (Figure 4B). The I_{300}/I_{360} ratio decreases with increasing D_{SEM}/D_{XRD} , i.e., with the increasing size of regular structural regions. Therefore, this correlation points that Lewis acidic sites are located in the defect area and formed by low-coordinated Zn atoms (Zn_{III} and Zn_{II})

Basic properties of ZIFs. Basicity of MAF-6 samples was investigated by DRIFT spectroscopy using deuterated chloroform ($CDCl_3$) as a C-H acid probe (DRIFT- $CDCl_3$). This method was successfully used to analyze the basicity of metal-organic frameworks, such as MIL-100(Al), Cu(BTC) and UiO-66 [59,60], NH_2 -UiO-66 [60], ZIF-8, and MAF-5 [37,39,60].

The spectra of $CDCl_3$ adsorbed on MAF-6 with different particle sizes are shown in Figures 5A and S7 (Supporting Information). Two bands at 2242 and 2250 cm^{-1} assigned to the interaction of $CDCl_3$ with basic sites (BS) can be distinguished. The strength of these bands as the proton affinity (PA) is 870 and 839 kJ/mol, respectively (Table 4). These values indicate that MAF-6 possesses lower basicity than that of 2-ethylimidazole (978 kJ/mol) [61]. The decreasing basicity of linker in ZIFs is due to the formation of a Zn-N bond via the interaction between Zn^{2+} and the nitrogen atom of the organic linker.

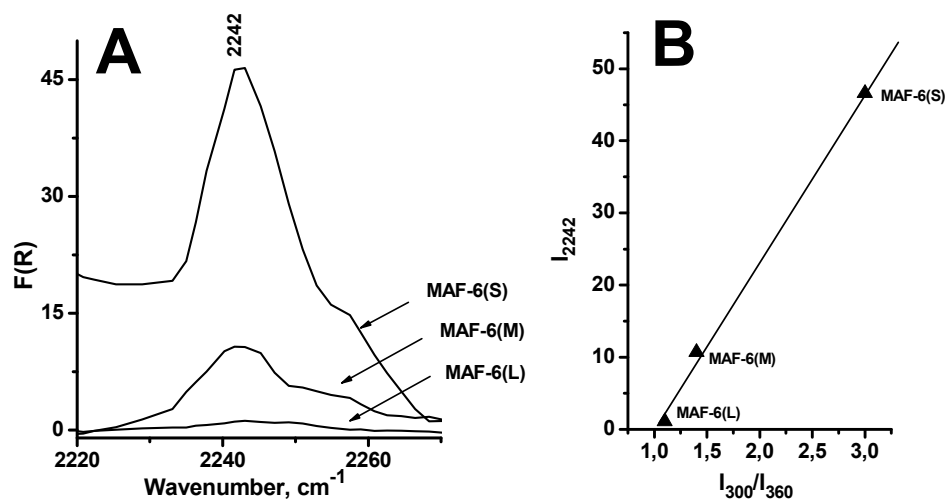


Figure 5. (A) DRIFT spectra of $CDCl_3$ adsorbed on MAF-6 with different particle sizes. (B) Correlation between I_{300}/I_{360} and the number of basic sites (I_{2242}).

Table 4. Basicity of different catalytic systems according to adsorption of CDCl_3 .

	$\nu_{\text{C-D}}$ (cm^{-1})	PA (kJ/mol)
CDCl_3	2268	-
2-Methylimidazole [61]	-	963.4
2-Ethylimidazole [61]	-	978
MAF-6	2250	839
	2242	870
MAF-5 [39]	2250	839
	2243	864
	2235	884
ZIF-8 [37]	2255	812
	2245	858
$\text{NH}_2\text{-UiO-66(Zr)}$ [60]	2253	839
	2245	867
UiO-66(Zr) [60]	2253	839

According to experimental data, particle size does not affect the strength of MAF-6 samples. Rather, the amount and accessibility of basic sites depend more on this parameter. Comparing the rate of CDCl_3 adsorption onto MAF-6, one can easily see the effect of particle size on the accessibility of basic sites (Figure S7, Supporting Information). When particle size decreases, the rate of CDCl_3 adsorption rises, i.e., sample with smaller particle faster uptakes CDCl_3 . Adsorption rate is dependent not only on particle size, but also on the microporosity of samples (V_{μ}/V_{Σ}) (Table 3) which affects the diffusion of CDCl_3 molecules inside the porous MAF-6 particle. Note that specific surface area and pore volume of MAF-6 samples play a minor role in the adsorption kinetics (Table 3). MAF-6(S) with 190 nm particle size has the highest adsorption rate despite of the lowest S_{BET} and total pore volume (V_{Σ}).

The particle size of MAF-6 affects the number of basic sites that following from the increasing integral intensity of the band at 2242 cm^{-1} (I_{2242}) with decreasing particle size of MAF-6 (Figure 4B). According to DFT calculations and different studies [58,62], basic sites are formed by Zn-OH groups and N-moieties of nonbridging linkers due to the existence of low-coordinated Zn atoms (Zn_{III} and Zn_{II}). This assertion agrees with the linear correlation between the intensity of band at 2242 cm^{-1} (I_{2242}) and the ratio of intensities of λ_{300} and λ_{360} (I_{300}/I_{360}) (Figure 5B). Note that decreasing the number of basic sites with increasing particle size is consistent with the changing of $D_{\text{SEM}}/D_{\text{XRD}}$ ratio (Figure 4B). The increasing size of regular structural regions leads to a decreasing number of basic sites.

It was interesting to compare the strength of basic sites of MAF-6 with that of ZIFs and MOFs reported in the literature. Data shown in Table 4 point that the basicity of ZIF-8 (858 kJ/mol) formed by 2-MIM is lower than that of MAF-6 (870 kJ/mol) formed by 2-EIM that is related to the lower basicity of 2-MIM than 2-EIM and the difference in pK_a of the conjugate acid for 2-MIM (7.85 [63,64]) and 2-EIM (8.0 [63,64]). At the same time, the basicity of MAF-5 also formed by 2-EIM is higher than that of MAF-6. We can suggest that this difference may be related to the high distortion of the framework of MAF-5 (Table S1, Supporting Information), which probably leads to changes in electron density in the basic sites. In general, basicity of ZIFs is higher than that of $\text{NH}_2\text{-UiO-66(Zr)}$ [60]. We can suggest that the low basicity of $\text{NH}_2\text{-UiO-66(Zr)}$ is due to the interaction strength between $-\text{NH}_2$ groups and carboxylic groups of the linker (2-amino-terephthalic acid).

2.2. Catalytic Properties of MAF-6

Catalytic properties of MAF-5 and MAF-6 were investigated in the cycloaddition of CO_2 to PO at 80 C under 0.8 MPa of CO_2 . The main results are shown in Tables 1 and 2. According to GC-MS analysis, PC was the major product with > 99% selectivity in all cases. A blank experiment pointed that the conversion of PO was << 1% after 5 h. In the presence

of MAF-5, the PO conversion increased to 8.2% (Table 1). After the addition of [n-Bu₄N]Br as co-catalyst, conversion of PO and yield of PC strongly rose (Table 2). The activity of MAF-5/[n-Bu₄N]Br binary system depended on the weight ratio of [n-Bu₄N]Br/MAF-5. The activity of binary system rose with increasing this ratio (Figure S8, Supporting Information). The maximal yield of PC was 66.6% at a ratio of 1/1, 80 °C for 5 h. The yield of PC rose to 79.9% with increasing reaction temperature from 80 to 100 °C. A kinetic profile of the coupling reaction of CO₂ with PO in the presence of MAF-5/[n-Bu₄N]Br (1/1) binary system is shown in Figure S8 (Supporting Information). It can be clearly seen that no induction period is observed in the kinetic curve for PC accumulation.

The addition of [n-Bu₄N]Br as co-catalyst had a similar effect on the reactivity of MAF-6 samples (Tables 1 and 2). Activities of [n-Bu₄N]Br/MAF-6 binary systems were higher in comparison with pristine MAF-6 samples. It is interesting that the catalytic performance of MAF-6 was higher in comparison with MAF-5. The lower yield of PC is not in agreement with the highest strength of basic sites of MAF-5 in comparison with MAF-6 (Table 4) which are important in reaction mechanism. According to a reaction mechanism (Scheme S1, Supporting Information), the Lewis acidic center interacts with the oxygen atom of the epoxide, while the Lewis basic site activates a CO₂ molecule [65,66]. Investigation of cycloaddition of CO₂ to PO by DRIFT spectroscopy pointed that the Zn-N couples (LAS-BS) are formed by the defect sites where proceeds ring-opening step and CO₂ activation [66]. The addition of [n-Bu₄N]Br to catalyst accelerates the ring-opening step due to the nucleophilic attack to C1 atom of epoxide and producing an intermediate (Scheme S1, Supporting Information).

The difference in activities of MAF-5 and MAF-6 can be caused by a few reasons. First, this phenomenon can be related to the difference in their structures (Table S1, Supporting Information). The MAF-5 with a zeolite ANA (Analcime) framework topology is formed by cells with the D3 (6²8³) symmetry, which have aperture (4.0 × 5.8 Å) and an elongated ellipsoidal cavity (7.0 × 10.0 Å) with windows of Zn₄(2-EIM)₄, Zn₆(2-EIM)₆ and Zn₈(2-EIM)₈ rings [49]. At the same time, the MAF-6 with a zeolite RHO framework topology has a large cavity (~18.7 Å) and aperture (~7.6 Å). Structure of MAF-6 is formed by cells with windows containing four-, six-, and eight-membered rings containing 48 Zn atoms per unit cell. Each cell is connected to six adjacent cells by means of polyhedral units, consisting of double eight-membered rings (known as D8R) [67]. The higher disorder of the framework and lower aperture size of MAF-5 in comparison with MAF-6 can lead to the decreasing accessibility of active sites for the reagents and increasing diffusion limitations. The other reason can be the difference in their textural properties (Table 3). Specific surface area and total pore volume of MAF-5 are lower in comparison with MAF-6 that can affect the number of active sites and therefore, activity.

Effect of particle size of MAF-6 samples in term of the PC yield was investigated in the presence and without [n-Bu₄N]Br at optimal experimental conditions (0.8 MPa of CO₂, 80 °C and 5 h) (Tables 1 and 2). Correlation between the crystal size of the MAF-6 material and the yield of PC is shown in Figure 6A. One can see the yield of PC decreased with increasing crystallite size. This phenomenon is caused by several reasons.

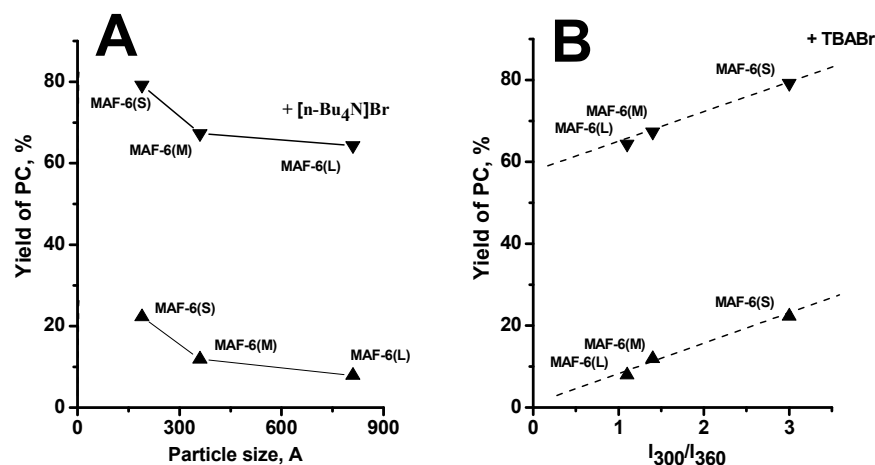


Figure 6. Dependence of PC yield on particle size of MAF-6 (A) and the number of Lewis acidic sites (I_{300}/I_{360}) (B).

First, the change in textural properties could affect the activity of MAF-6. The simultaneous increase in microporosity (V_{μ}/V_{Σ}) and particle size of the MAF-6 material (Table 3) gives rise to the reduction of activity due to the rising diffusion limitations. This trend can point that mesopores are beneficial for the high catalytic activity of MAF-6 and ZIFs materials in general.

The varying amount and localization of active sites can be another reason of the dependence of activity MAF-6 on crystal size. Correlation between the yield of PC and the number of Lewis acidic sites (I_{300}/I_{360}) is shown in Figure 6B. One can see that the yield of PC rises with increasing amount active sites formed by low-coordinated Zn atoms (Zn_{III} and Zn_{II}). The yield of PC also increases with increasing the number of basic sites (I_{2242}) of the MAF-6 material (Figure S9, Supporting Information). Both correlations indicate that both LAS and BS play an important role in the reaction mechanism. The high yield of PC could be obtained in the presence of MAF-6 sample containing a large number of active centers. These trends are in agreement with the structure and textural properties of MAF-6 samples. The low activity of MAF-6(L) with large particle size is due to the low quantity of active sites that is derived from the high structural order of particles. Such interdependence indicates that active sites are formed by defects and located in the regions close to the surface of the crystallites. This suggestion is confirmed by linear correlation between yield of PC and D_{SEM}/D_{XRD} ratio (Figure S10, Supporting Information). The interdependence between defects and active sites, and impact of active sites on the catalytic performance were demonstrated for ZIF-8 [37,68].

2.3. Stability and Efficiency of MAF-6

The stability of MAF-6 in the course of the reaction was investigated by SEM. SEM images of MAF-6(L) and MAF-6(S) samples, after application in catalytic reaction, are shown in Figure 7. Mechanical degradation of the MAF-6 (L) crystals was observed due to a result of stirring. At the same time, similar mechanical degradation of the MAF-6 (S) crystals was found. The damage of the MAF-6(S) structure was confirmed by elemental analysis which pointed to the Zn^{2+} leaching due to the polar reagents and intermediates. Amount Zn^{2+} leached from MAF-6(S) was ~1.43 wt%. Note that this amount of Zn^{2+} leached did not affect the catalytic activity of MAF-6(S). The size effect on the stability of ZIF-8 samples towards etching and Zn^{2+} leaching was also observed in the Knöevenagel condensation reaction and the transesterification of hexanol and vinyl acetate [68].

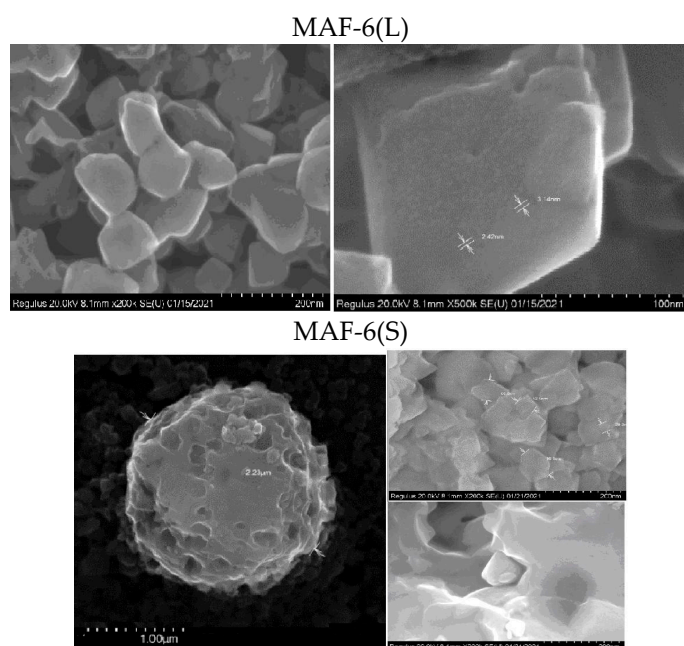


Figure 7. SEM images of MAF-6 samples with different particle size after catalytic test in reaction of propylene oxide with CO₂.

The comparison catalytic performance of the most active system (MAF-6(S)/[n-Bu₄N]Br) with ZIFs/[n-Bu₄N]Br systems, which had been reported in literature, are shown in Table 2. One can see from these data all systems are active at sufficiently near and mild conditions at 0.8–1.2 MPa of CO₂ and 80–120 °C. Despite of the difference in CO₂ pressure, we can say that efficiency of MAF-6(S)/[n-Bu₄N]Br system is superior to ZIF-23/[n-Bu₄N]Br and very close to the ZIF-95/[n-Bu₄N]Br. Note that the catalytic performance of MAF-5/[n-Bu₄N]Br is also higher than ZIF-23/[n-Bu₄N]Br both at 80 and 100 °C. MAF-5/[n-Bu₄N]Br allows to obtain PC with 80.7% yield at 100 °C, while in the presence of ZIF-23/[n-Bu₄N]Br yield of PC is only 61.7% at 120 °C

3. Materials and Methods

3.1. Materials

Propylene oxide (>98%, Acros Organics) and [n-Bu₄N]Br (Sigma-Aldrich) were used without further purification. Zn(NO₃)₂·6H₂O, 2-ethylimidazole (2-EIM) were purchased from Acros Organic.

MAF-5 was synthesized from 2-EIM and Zn(NO₃)₂·6H₂O according to the method described in Ref. [69]. The main textural and physicochemical properties are show in Figures S1–S3 (Supporting Information).

MAF-6 samples were synthesized from 2-EIM and [Zn(NH₃)₄](OH)₂ according to the method described in [70] after a small modification. 2-EIM (4 mmol) was dissolved in mixed solvent systems (alcohol/cyclohexane). Zn(OH)₂ (2 mmol), which was dissolved in aqueous NH₃ (25%) solution (30 ml), was added once to the above described 2-EIM solution. MAF-6 samples were obtained after vigorous stirring of the reaction mixture for 20 min under room temperature. The main experimental conditions for synthesis of MAF-6 samples, properties of solvents, particle size, and textural properties of materials are shown in Table 3. The main textural and physicochemical properties are show in Figures S4–S8 (Supporting Information).

3.2. Instrumental Measurements

X-ray diffraction (XRD) patterns were obtained with the use of a Thermo ARL X'tra device, with the CuKα-radiation (λ = 1.5418 Å), focusing geometry θ–2θ in the scanning mode within the range of angles of 2θ from 3 to 75° with the step of 0.05°.

The textural characteristics of the MAF-5 and MAF-6 samples were determined from the adsorption isotherm of N₂ at −196 °C using a Micromeritics ASAP 2400. Chemical analyses were done by an inductively coupled plasma-atomic emission spectrometry (ICP-AES) using a PERKIN-ELMER instrument OPTIMA 4300.

Scanning electron microscopy (SEM) images were obtained with a Hitachi Regulus microscope operated at an accelerating voltage of 20 kV in secondary electron mode. The size distribution of the nanoparticles was calculated based on a representative set of SEM images taken at different areas of the sample.

The basicity of ZIFs was determined by DRIFT spectroscopy with CDCl₃ as probe molecule to follow the technique that was explained in [71].

DRIFT spectra were recorded on a Shimadzu FTIR-8300S spectrometer with a DRS-8000 diffusion reflectance cell in the range between 400 and 6000 cm^{−1} with a resolution of 4 cm^{−1}. All spectra are presented in F(R) Kubelka–Munk scale: $F(R) = \frac{(1-R)^2}{2R}$, where R is reflection coefficient. The DR-UV-Vis spectra were recorded on a UV-2501 PC Shimadzu spectrometer with an IRS-250A accessory in the 190–900 nm range with a resolution of 2 nm, on samples in powder form placed into a special cell for DR-UV-Vis measurement. BaSO₄ was used as standard for measurements.

4. Conclusions

In this work, zeolitic imidazolate frameworks MAF-5 and MAF-6 were demonstrated to be effective catalysts in the cycloaddition of CO₂ to propylene oxide to propylene carbonate (without any solvent) at 0.8 MPa of CO₂ and 80 °C. The activity of MAFs/[n-Bu₄N]Br binary systems depended on the weight ratio of [n-Bu₄N]Br/MAFs. The activity of binary systems rose with increasing this ratio. The maximal yields of PC were 80.5 and 66.6% at a ratio of 1/1, 80 °C for 5 h in the presence of MAF-6/[n-Bu₄N]Br and MAF-5/[n-Bu₄N]Br, respectively. Lower activity of MAF-5 in comparison with MAF-6 could be caused by the difference in their structural and textural characteristics which affect the accessibility of active sites for the reagents and increasing diffusion limitations.

Size effect on the reaction rate and yield of propylene carbonate was investigated in the presence of MAF-6. MAF-6 samples with particle size of 190 ± 20, 360 ± 30, and 810 ± 30 nm (MAF-6(S), MAF-6(M), and MAF-6(L), respectively) were prepared at room temperature from [Zn(NH₃)₄](OH)₂ and 2-ethylimidazole. Particle size was controlled by variation of type of alcohol in alcohol/cyclohexane media. Particle size reduced in the order: MeOH > EtOH > PrOH. According to comprehensive study, textural properties, and the type and content of active sites, depend on the particle sizes of MAF-6 samples. The catalytic activity of MAF-6 rose with decreasing particle size due to the increasing number and location of active sites in surface of solid. Maximal yield of PC was observed in the presence of MAF-6(S). Results of this investigation indicated that mesopores are beneficial to the high catalytic activity of MAFs and ZIFs materials in general.

Particle size also affects the stability of MAF-6 crystals. SEM data pointed that in contrast to MAF-6(L), MAF-6(S) sample is exposed to the indiscriminate etching of surface of crystal due to the leaching of Zn²⁺ by polar reagents. The efficiencies of MAFs/[n-Bu₄N]Br binary systems were compared with that of ZIFs/[n-Bu₄N]Br reported in the literature. It was found that activity of MAFs were comparable and higher under similar reaction conditions.

Supplementary Materials: The following are available online at <https://www.mdpi.com/article/10.3390/catal11091061/s1>, Figure S1: SEM image of MAF-5, Figure S2: Isotherms of N₂ adsorption-desorption onto MAF-5, Figure S3: XRD pattern of MAF-5, Figure S4: Isotherms of N₂ adsorption-desorption onto MAF-5 and MAF-6 samples, Figure S5: DRIFT spectra of MAF-6 with different particle size, Figure S6: DR-UV-vis spectra of MAF-6(L) and MAF-6(S) after calcination at 150 °C for 2 h in vacuum and the next addition of wet air, Figure S7: (A–C) DRIFT spectra of CDCl₃ adsorbed on MAF-6 samples with different particle size. (D) The change of integral intensity of band at 2242 cm^{−1} in the course of adsorption of CDCl₃; Figure S8: (A) Kinetic curve of propylene carbonate accumulation in the presence of MAF-5 (Experimental conditions: 24 mmol of propylene

oxide, 8 atm of CO₂ (at room temperature), 0.85 mmol MAF-5, 0.85 mmol of [n-Bu₄N]Br, 80 °C). (B) Effect of [n-Bu₄N]Br amount in reaction mixture on yield of propylene carbonate in the presence of MAF-5 (Experimental conditions: 24 mmol of propylene oxide, 8 atm of CO₂ (at room temperature), 0.85 mmol of catalyst, 80 °C, 5 h), Figure S9: Dependence of PO conversion on the number of basic sites (I₂₂₄₂), Figure S10: Dependence of PO conversion on the ratio of D_{SEM}/D_{X-ray}, Table S1: Structural properties of ZIF-8, MAF-5 and MAF-6, Table S2: MAF-6 particle size estimated from XRD and SEM data, Scheme S1: Mechanisms of reaction between propylene oxide and CO₂.

Author Contributions: Conceptualization, S.H.J. and M.N.T.; preparation of samples, XRD and texture investigation, B.N.B.; DR-UV-Vis and DRIFT spectroscopy, V.N.P., catalytic investigations, I.A.L.; SEM investigation, E.Y.G.; writing—original draft preparation, M.N.T.; writing—review and editing, S.H.J. and V.N.P.; funding acquisition, S.H.J. All authors have read and agreed to the published version of the manuscript.

Funding: This work was supported by the National Research Foundation of Korea (NRF) grant funded by the Korea government (MSIT) (Grant number: NRF-2020R1A4A1018393) and the Ministry of Science and Higher Education of the Russian Federation within the governmental order for Borekov Institute of Catalysis (AAAA-A21-121011390055-8).

Acknowledgments: Authors thanks S.V. Tsybulya for the discussion of XRD data.

Conflicts of Interest: The authors declare no conflict of interest.

References

1. National Academies of Sciences, Engineering, and Medicine. Chemical Utilization of CO₂ into Chemicals and Fuels. In *Gaseous Carbon Waste Streams Utilization: Status and Research Needs*; The National Academies Press: Washington, DC, USA, 2019.
2. Quadrelli, E.A.; Centi, G.; Duplan, J.-L.; Perathoner, S. Carbon dioxide recycling: Emerging large-scale technologies with industrial potential. *ChemSusChem* **2011**, *4*, 1194–1215. [CrossRef]
3. Artz, J.; Müller, T.E.; Thenert, K.; Kleinekorte, J.; Meys, R.; Sternberg, A.; Bardow, A.; Leitner, W. Sustainable conversion of carbon dioxide: An integrated review of catalysis and life cycle assessment. *Chem. Rev.* **2018**, *118*, 434–504. [CrossRef] [PubMed]
4. Aresta, M.; Nocito, F.; Dibenedetto, A. What catalysis can do for boosting CO₂ utilization. *Adv. Catal.* **2018**, *62*, 49–109.
5. *VCI & DECHEMA Position Paper Utilization and Storage of CO₂*; DECHEMA: Frankfurt, Germany, 2009.
6. Suib, S.L. (Ed.) *New and Future Developments in Catalysis: Activation of Carbon Dioxide*; Elsevier: Amsterdam, The Netherlands, 2013.
7. Bhanage, B.M.; Arai, M. (Eds.) *Transformation and Utilization of Carbon Dioxide*; Springer: New York, NY, USA, 2014.
8. NexantECA. Market Analytics: Ammonia and Urea. Available online: <https://www.nexanteca.com/news-and-media/new-analysis-market-analytics-ammonia-and-urea-2020-0> (accessed on 10 August 2021).
9. ADROIT Market Research: Salicylic Acid Market. Available online: <https://www.adroitmarketresearch.com/infographics/salicylic-acid-industry> (accessed on 10 August 2021).
10. Fukuoka, S.; Kawamura, M.; Komiyama, K.; Tojo, M.; Hachiya, H.; Hasegawa, K.; Aminaka, M.; Okamoto, H.; Fukawa, I.; Konno, S. A novel non-phosgene polycarbonate production process using by-product CO₂ as starting material. *Green Chem.* **2003**, *5*, 497–507. [CrossRef]
11. Langanke, J.; Wolf, A.; Hofmann, J.; Böhm, K.; Subhani, M.A.; Müller, T.E.; Leitner, W.; Gürtler, C. Carbon dioxide (CO₂) as sustainable feedstock for polyurethane production. *Green Chem.* **2014**, *16*, 1865–1870. [CrossRef]
12. Allied Market Research: Ethylene Carbonate Market. Available online: <https://www.alliedmarketresearch.com/ethylene-carbonate-market-A07307> (accessed on 10 August 2021).
13. Market.us: Propylene Carbonate Market. Available online: <https://market.us/report/propylene-carbonate-market> (accessed on 30 August 2021).
14. Kamphuis, A.J.; Picchioni, F.; Pescarmona, P.P. CO₂-fixation into cyclic and polymeric carbonates: Principles and applications. *Green Chem.* **2019**, *21*, 406–448. [CrossRef]
15. Lopes, E.J.C.; Ribeiro, A.P.C.; Martins, L.M.D.R.S. New trends in the conversion of CO₂ to cyclic carbonates. *Catalysts* **2020**, *10*, 479. [CrossRef]
16. Yano, T.; Matsui, H.; Koike, T.; Ishiguro, H.; Fujihara, H.; Yoshihara, M.; Maeshima, T. Magnesium oxide-catalysed reaction of carbon dioxide with an epoxide with retention of stereo chemistry. *Chem Commun.* **1997**, 1129, 1130.
17. Bhanage, B.M.; Fujita, S.; Ikushima, Y.; Torii, K.; Arai, M. Synthesis of dimethyl carbonate and glycols from carbon dioxide, epoxides and methanol using heterogeneous basic metal oxide catalysts with high activity and selectivity. *Appl. Catal. A Gen.* **2001**, *219*, 259–266. [CrossRef]
18. Welton, T. Room-temperature ionic liquids. Solvents for synthesis and catalysis. *Chem. Rev.* **1999**, *99*, 2071–2083. [CrossRef] [PubMed]
19. Martins, M.A.P.; Frizzo, C.P.; Moreira, D.N.; Zanatta, N.; Bonacorso, H.G. Ionic liquids in heterocyclic synthesis. *Chem. Rev.* **2008**, *108*, 2015–2050. [CrossRef]

20. Sun, J.; Fujita, S.; Arai, M. Development in the green synthesis of cyclic carbonate from carbon dioxide using ionic liquids. *J. Organomet. Chem.* **2005**, *690*, 3490–3497. [[CrossRef](#)]
21. Lan, D.H.; Fan, N.; Wang, Y.; Gao, X.; Zhang, P.; Chen, L.; Au, C.T.; Yin, S.F. Recent advances in metal-free catalysts for the synthesis of cyclic carbonates from CO₂ and epoxides. *Chin. J. Catal.* **2016**, *37*, 826–845. [[CrossRef](#)]
22. Girard, A.L.; Simon, N.; Zanatta, M.; Marmitt, S.; Goncalves, P.; Dupont, J. Insights on recyclable catalytic system composed of task-specific ionic liquids for the chemical fixation of carbon dioxide. *Green Chem.* **2014**, *16*, 2815–2825. [[CrossRef](#)]
23. Beyzavi, M.H.; Stephenson, C.J.; Liu, Y.; Karagiari, O.; Hupp, J.T.; Farha, O.K. Metal-organic framework-based catalysts: Chemical fixation of CO₂ with epoxides leading to cyclic organic carbonates. *Front. Energy Res.* **2015**, *2*, 10. [[CrossRef](#)]
24. He, H.; Perman, J.A.; Zhu, G.; Ma, S. Metal-organic frameworks for CO₂ chemical transformations. *Small* **2016**, *12*, 6309–6324. [[CrossRef](#)]
25. Song, J.; Zhang, Z.; Hu, S.; Wu, T.; Jiang, T.; Han, B. MOF-5/*n*-Bu₄NBr: An efficient catalyst system for the synthesis of cyclic carbonates from epoxides and CO₂ under mild conditions. *Green Chem.* **2009**, *11*, 1301–1336. [[CrossRef](#)]
26. Xiang, W.; Shen, C.; Lu, Z.; Chen, S.; Li, X.; Zou, R.; Zhang, Y.; Liu, C. CO₂ cycloaddition over ionic liquid immobilized hybrid zeolitic imidazolate frameworks: Effect of Lewis acid/base sites. *Chem. Eng. Sci.* **2021**, *233*, 116429. [[CrossRef](#)]
27. Ryu, H.; Roshan, R.; Kim, M.-I.; Kim, D.-W.; Selvaraj, M.; Park, D.-W. Cycloaddition of carbon dioxide with propylene oxide using zeolitic imidazolate framework ZIF-23 as a catalyst. *Korean J. Chem. Eng.* **2017**, *34*, 928–934. [[CrossRef](#)]
28. Tharun, J.; Mathai, G.; Kathalikkatti, A.C.; Roshan, R.; Won, Y.-S.; Cho, S.J.; Chang, J.-S.; Park, D.-W. Exploring the catalytic potential of ZIF-90: Solventless and Co-Catalyst-Free Synthesis of propylene carbonate from propylene oxide and CO₂. *Chem Plus Chem.* **2015**, *80*, 715–721. [[CrossRef](#)] [[PubMed](#)]
29. Tharun, J.; Bhin, K.-M.; Roshan, R.; Kim, D.W.; Kathalikkattil, A.C.; Babu, R.; Ahn, H.Y.; Won, Y.S.; Park, D.-W. Ionic liquid tethered post functionalized ZIF-90 framework for the cycloaddition of propylene oxide and CO₂. *Green Chem.* **2016**, *18*, 2479–2487. [[CrossRef](#)]
30. Jose, T.; Hwang, Y.; Kim, D.-W.; Kim, M.-I.; Park, D.-W. Functionalized zeolitic imidazolate framework F-ZIF-90 as efficient catalyst for the cycloaddition of carbon dioxide to allyl glycidyl ether. *Catal. Today* **2015**, *245*, 61–67. [[CrossRef](#)]
31. Bhin, K.M.; Tharun, J.; Roshan, K.R.; Kim, D.-W.; Chung, Y.; Park, D.-W. Catalytic performance of zeolitic imidazolate framework ZIF-95 for the solventless synthesis of cyclic carbonates from CO₂ and epoxides. *J. CO₂ Util.* **2017**, *17*, 112–118. [[CrossRef](#)]
32. Kuruppathparambil, R.R.; Babu, R.; Jeong, H.; Hwang, G.-Y.; Jeong, G.S.; Kim, M.-I.; Dong-Kim, W.; Park, D.-W. A solid solution zeolitic imidazolate framework as a room temperature efficient catalyst for the chemical fixation of CO₂. *Green Chem.* **2016**, *18*, 6349–6356. [[CrossRef](#)]
33. Babu, R.; Kathalikkattil, A.C.; Roshan, R.; Tharun, J.; Kim, D.W.; Park, D.W. Dual-porous metal organic framework for room temperature CO₂ fixation via cyclic carbonate synthesis. *Green Chem.* **2016**, *18*, 232–242. [[CrossRef](#)]
34. Hu, L.; Yan, Z.; Mo, X.; Peng, X.; Chen, L. Morphology control synthesis of ZIF-8 as highly efficient catalyst for the cycloaddition of CO₂ to cyclic carbonate. *ChemCatChem.* **2019**, *11*, 3212–3219. [[CrossRef](#)]
35. Schejn, A.; Balan, L.; Falk, V.; Aranda, V.; Medjahdi, L.; Schneider, G.; Schneider, R. Controlling ZIF-8 nano- and microcrystal formation and reactivity through zinc salt variations. *Cryst. Eng. Comm.* **2014**, *16*, 4493–4500. [[CrossRef](#)]
36. Zhang, F.; Wei, Y.; Wu, X.; Jiang, H.; Wang, W.; Li, H. Hollow zeolitic imidazolate framework nanospheres as highly efficient cooperative catalysts for [3+3] cycloaddition reactions. *J. Am. Chem. Soc.* **2014**, *136*, 13963–13966. [[CrossRef](#)]
37. Timofeeva, M.; Paukshtis, E.; Panchenko, V.; Shefer, K.; Isaeva, V.; Kustov, L.; Gerasimov, E. Tuning the catalytic performance of the novel composites based on ZIF-8 and Nafen through dimensional and concentration effects in the synthesis of propylene glycol methyl ether. *Eur. J. Org. Chem.* **2019**, *26*, 4215–4225. [[CrossRef](#)]
38. Timofeeva, M.N.; Panchenko, V.N.; Lukoyanov, I.A.; Jhung, S.H. Proceedings of the 2nd International Conference on Reaction Kinetics, Mechanisms and Catalysis, Budapest, Hungary, 20–22 May 2021.
39. Timofeeva, M.N.; Lykoyanov, I.A.; Panchenko, V.N.; Shefer, K.I.; Bhadra, B.N.; Jhung, S.H. Zeolitic imidazolate frameworks ZIF-8 and MAF-5 as highly efficient heterogeneous catalysts for synthesis of 1-methoxy-2-propanol from methanol and propylene oxide. *Ind. Eng. Chem. Res.* **2019**, *58*, 10750–10758. [[CrossRef](#)]
40. Bustamante, E.; Fernandez, J.L.; Zamaro, J.M. Influence of the solvent in the synthesis of zeolitic imidazolate framework-8 (ZIF-8) nanocrystals at room temperature. *J. Colloid. Interface Sci.* **2014**, *424*, 37–43. [[CrossRef](#)]
41. Marcus, Y. The Effectiveness of solvents as hydrogen bond donors. *J. Solut. Chem.* **1991**, *20*, 929–944. [[CrossRef](#)]
42. Park, K.S.; Ni, Z.; Côté, A.P.; Choi, J.Y.; Huang, R.; Uribe-Romo, F.J.; Chae, H.K.; O’Keeffe, M.; Yaghi, O.M. Exceptional chemical and thermal stability of zeolitic imidazolate frameworks. *Proc. Natl. Acad. Sci. USA* **2006**, *103*, 10186–10191. [[CrossRef](#)] [[PubMed](#)]
43. Self, K.; Telfer, M.; Greer, H.F.; Zhou, W. Reversed crystal growth of RHO zeolitic imidazolate framework (ZIF). *Chem. Eur. J.* **2015**, *21*, 19090–19095. [[CrossRef](#)]
44. Mortada, B.; Chaplais, G.; Nouali, H.; Marichal, C.; Patarin, J. Phase transformations of Metal-Organic Frameworks MAF-6 and ZIF-71 during intrusion-extrusion experiments. *J. Phys. Chem. C* **2019**, *123*, 4319–4328. [[CrossRef](#)]
45. Gao, M.; Wang, J.; Rong, Z.; Shi, Q.; Dong, J. A combined experimental-computational investigation on water adsorption in various ZIFs with the SOD and RHO topologies. *RSC Adv.* **2018**, *8*, 39627–39634. [[CrossRef](#)]
46. Abdel-wahab, M.S.; Jilani, A.; Yahia, I.S.; Al-Ghamdi, A.A. Enhanced the photocatalytic activity of Ni-doped ZnO thin films: Morphological, optical and XPS analysis. *Superlatt. Microstruct.* **2016**, *94*, 108–118. [[CrossRef](#)]

47. Jilani, A.; Abdel-wahab, M.S.; Al-ghamdi Attieh, A.; Dahlan, A.; Sadik Yahia, I.S. Nonlinear optical parameters of nanocrystalline AZO thin film measured at different substrate temperatures. *Phys. B Condens. Matter* **2016**, *481*, 97–103. [CrossRef]
48. Bettens, B.; Dekeyser, S.; van der Bruggen, B.; Degreve, J.; Vandecasteele, C. Transport of pure components in pervaporation through a microporous silica membrane. *J. Phys. Chem. B* **2005**, *109*, 5216–5222. [CrossRef]
49. Huang, X.-C.; Lin, Y.-Y.; Zhang, J.-P.; Chen, X.-M. Ligand-directed strategy for zeolite-type metal-organic frameworks: Zinc(II) imidazolates with unusual zeolitic topologies. *Angew. Chem. Int. Ed.* **2006**, *45*, 1557–1559. [CrossRef]
50. Tanaka, S.; Fujita, K.; Miyake, Y.; Miyamoto, M.; Hasegawa, Y.; Makino, T.; van der Perre, S.; Remi, J.C.S.; van Assche, T.; Baron, G.V.; et al. Adsorption and diffusion phenomena in crystal size engineered ZIF-8 MOF. *J. Phys. Chem. C* **2015**, *119*, 28430–28439. [CrossRef]
51. Zhang, C.; Gee, J.A.; Sholl, D.S.; Lively, R.P. Crystal-size-dependent structural transitions in nanoporous crystals: Adsorption-induced transitions in ZIF-8. *J. Phys. Chem. C* **2014**, *118*, 20727–20733. [CrossRef]
52. Karaagas, D.; Kurkcuoglu, G.S. Synthesis and characterizations of the cyanide-bridged heteronuclear polymeric complexes with 2-ethylimidazole. *Bull. Chem. Soc. Ethiop.* **2016**, *30*, 263–272. [CrossRef]
53. Arivazhagan, M.; Manivel, S.; Jeyavijayan, S.; Meenakshi, R. Vibrational spectroscopic (FTIR and FT-Raman), first-order hyperpolarizability, HOMO, LUMO, NBO, Mulliken charge analyses of 2-ethylimidazole based on Hartree-Fock and DFT calculations. *Spectrochim. Acta A Mol. Biomol. Spectrosc.* **2015**, *134*, 493–501. [CrossRef]
54. Zhang, C.; Han, C.; Sholl, D.S.; Schmidt, J.R. Computational characterization of defects in metal-organic frameworks: Spontaneous and water induced point defects in ZIF-8. *J. Phys. Chem. Lett.* **2016**, *7*, 459–464. [CrossRef]
55. Trivedi, M.K.; Branton, A.; Trivedi, D.; Nayak, G.; Saikia, G.; Jana, S. Physical and structural characterization of biofield treated imidazole derivatives. *Nat. Prod. Chem. Res.* **2015**, *3*, 187–195. [CrossRef]
56. Godlewska, S.; Jezierska, J.; Baranowska, K.; Augustin, E.; Dołęga, A. Copper(II) complexes with substituted imidazole and chlorido ligands: X-ray, UV-Vis, magnetic and EPR studies and chemotherapeutic potential. *Polyhedron* **2013**, *65*, 288–297. [CrossRef]
57. Isaia, F.; Aragoni, M.C.; Arca, M.; Bettoschi, A.; Caltagirone, C.; Castellano, C.; Demartin, F.; Lippolis, V.; Pivetta, T.; Valletta, E. Zinc(II)-methimazole complexes: Synthesis and reactivity. *Dalton. Trans.* **2015**, *44*, 9805–9814. [CrossRef]
58. Chizallet, C.; Lazare, S.; Bazer-Bachi, D.; Bonnier, F.; Lecocq, V.; Soyer, E.; Quoineaud, A.-A.; Bats, N. Catalysis of transesterification by a nonfunctionalized metal-organic framework: Acid-basicity at the external surface of ZIF-8 probed by FTIR and *ab Initio* calculations. *J. Am. Chem. Soc.* **2010**, *132*, 12365–12377. [CrossRef]
59. Timofeeva, M.N.; Panchenko, V.N.; Jun, J.W.; Hasan, Z.; Matrosova, M.M.; Jhung, S.H. Effects of linker substitution on catalytic properties of porous zirconium terephthalate UiO-66 in acetalization of benzaldehyde with methanol. *Appl. Catal. A Gen.* **2014**, *471*, 91–97. [CrossRef]
60. Panchenko, V.N.; Matrosova, M.M.; Jeon, J.; Jun, J.W.; Timofeeva, M.N.; Jhung, S.H. Catalytic behavior of metal-organic frameworks in the Knoevenagel condensation reaction. *J. Catal.* **2014**, *316*, 251–259. [CrossRef]
61. The National Institute of Standards and Technology (NIST) Is an Agency of the U.S. Commerce Department. Available online: <https://webbook.nist.gov> (accessed on 20 October 2018).
62. Ueda, T.; Nakai, M.; Yamatani, T. A solid-state ¹H-NMR study of the dynamic structure of ZIF-8 and its role in the adsorption of bulky molecules. *Adsorption* **2017**, *23*, 887–901. [CrossRef]
63. Parlie, D.; Thiubaut, D.; Caude, M.; Rosset, R. Supercritical fluid chromatography of imidazole derivatives. *Chromatographia* **1991**, *31*, 293–296. [CrossRef]
64. Matuszak, C.A.; Matuszak, A.J. Imidazole-versatile today, prominent tomorrow. *J. Chem. Educ.* **1976**, *53*, 280–284. [CrossRef]
65. Mori, K.; Mitani, Y.; Hara, T.; Mizugaki, T.; Ebitani, K.; Kaneda, K. A single-site hydroxyapatite-bound zinc catalyst for highly efficient chemical fixation of carbon dioxide with epoxides. *Chem. Commun.* **2005**, 3331, 3333.
66. Vitillo, J.G.; Crocella, V.; Bonino, F. ZIF-8 as a catalyst in ethylene oxide and propylene oxide reaction with CO₂ to cyclic organic carbonates. *Chem. Eng.* **2019**, *3*, 60. [CrossRef]
67. Biswal, B.P.; Panda, T.; Banerjee, R. Solution mediated phase transformation (RHO to SOD) in porous Co-imidazolate based zeolitic frameworks with high water stability. *Chem. Commun.* **2012**, *48*, 11868–11870. [CrossRef] [PubMed]
68. Linder-Patton, O.M.; de Prinse, T.J.; Furukawa, S.; Bell, S.G.; Sumida, K.; Doonan, C.J.; Sumbly, C.J. Influence of nanoscale structuralisation on the catalytic performance of ZIF-8: A cautionary surface catalysis study. *Cryst. Eng. Comm.* **2018**, *20*, 4926–4934. [CrossRef]
69. Bhadra, B.N.; Seo, P.W.; Khan, N.A.; Jhung, S.H. Hydrophobic cobalt-ethylimidazolate frameworks: Phase-pure syntheses and possible application in cleaning of contaminated water. *Inorg. Chem.* **2016**, *55*, 11362–11371. [CrossRef] [PubMed]
70. He, C.-T.; Jiang, L.; Ye, Z.-M.; Krishna, R.; Zhong, Z.-S.; Liao, P.-Q.; Xu, J.; Ouyang, G.; Zhang, J.-P.; Chen, X.-M. Exceptional hydrophobicity of a large-pore metal-organic zeolite. *J. Am. Chem. Soc.* **2015**, *137*, 7217–7223. [CrossRef]
71. Paukshtis, E.A.; Kotsarenko, N.S.; Karakchiev, L.G. Investigation of proton-acceptor properties of oxide surfaces by IR spectroscopy of hydrogen-bonded complexes. *React. Kinet. Catal. Lett.* **1979**, *12*, 315–319. [CrossRef]